This is the pre-peer reviewed version of the following article:

Zhao W., Kim J., Huang X., Zhang L., Pesquera D., Velarde G.A.P., Gosavi T., Lin C.-C., Nikonov D.E., Li H., Young I.A., Ramesh R., Martin L.W.. Low-Voltage Magnetoelectric Coupling in Fe0.5Rh0.5/0.68PbMg1/3Nb2/3O3-0.32PbTiO3 Thin-Film Heterostructures. Advanced Functional Materials, (2021). . : - . 10.1002/adfm.202105068,

which has been published in final form at https://dx.doi.org/10.1002/adfm.202105068. This article may be used for non-commercial purposes in accordance with Wiley Terms and Conditions for Use of Self-Archived Versions.

Low-Voltage Magnetoelectric Coupling in $Fe_{0.5}Rh_{0.5}$/ $0.68PbMg_{1/3}Nb_{2/3}O_3$-$0.32PbTiO_3$ Thin-Film Heterostructures

Wenbo Zhao[1*], Jieun Kim[1*], Xiaoxi Huang[1], Lei Zhang[1], David Pesquera[1,4], Gabriel A. P. Velarde[1], Tanay Gosavi[3], Chia-Ching Lin[3], Dmitri E. Nikonov[3], Ian A. Young[3], Ramamoorthy Ramesh[1,2], Lane W. Martin[1,2,†]

[1] Department of Materials Science and Engineering, University of California, Berkeley, CA, USA

[2] Materials Sciences Division, Lawrence Berkeley National Laboratory, Berkeley, CA, USA

[3] Components Research, Intel Corporation, Hillsboro, OR, USA

[4] Catalan Institute of Nanoscience and Nanotechnology (ICN2), CSIC and BIST, Campus UAB, Bellaterra, 08193 Barcelona, Spain

* These authors contributed equally to the work; [†] lwmartin@berkeley.edu

ABSTRACT

The rapid development of computing applications demands novel low-energy consumption devices for information processing. Among various candidates, magnetoelectric heterostructures hold promise for meeting the required voltage and power goals. Here, we demonstrate a route to low-voltage control of magnetism in 30 nm $Fe_{0.5}Rh_{0.5}$/100 nm $0.68PbMg_{1/3}Nb_{2/3}O_3$-$0.32PbTiO_3$ (PMN-PT) heterostructures wherein the magnetoelectric coupling is achieved via strain-induced changes in the $Fe_{0.5}Rh_{0.5}$ mediated by voltages applied to the PMN-PT. We describe approaches to achieve high-quality, epitaxial growth of $Fe_{0.5}Rh_{0.5}$ on the PMN-PT films and, a methodology to probe and quantify magnetoelectric coupling in small thin-film devices via anomalous Hall effect

studies. By comparing the spin-flop field change induced by temperature and external voltage, the magnetoelectric coupling coefficient is estimated to reach ~7.08 x 10^{-8} s/m at 325 K while applying a -0.75 V bias.

KEYWORDS: Multiferroic heterostructures; Piezo-strain effect; Magnetoelectric coupling; Non-volatile; anomalous hall effect.

INTRODUCTION

Moore's Law[1] and Dennard scaling[2] have been important guiding principles in the semiconductor industry. With the continued decrease of critical dimensions in logic and memory devices, however, there has been an increasing challenge to meet the requirements of these guiding principles, raising important challenges for the future of integrated circuit (IC) design.[3] The strong desire to identify beyond-CMOS devices and technologies[4–6] has driven increasing attention to a range of alternative computing platforms, including systems based on electron,[7–9] spin,[10,11] ferroelectric,[12] strain,[13] and other phenomena to overcome the "Boltzmann Tyranny" in electronic systems. Spin-based logic has emerged as one of the leading options[4,6] due to an intriguing combination of non-volatility, higher logic efficiency,[14] and the potential for built-in memory-in-logic and/or logic-in-memory function. Traditional spin-logic devices, however, have limitations – including large energy dissipation during current-driven magnetic field or spin-transfer torque generation and the fast spin decoherence of many semiconductors results from spin-orbit coupling.[15]

Recently, a magnetoelectric spin-orbit (MESO) logic-in-memory device has been proposed to address these challenges.[16] Taking advantage of the fact that a charge input/output is easier to accomplish, the input signal in the MESO device is a voltage input that is converted by the

magnetoelectric into a spin signal. After the logic operations are completed in the spin domain, the spin is then back-converted to a charge signal using the inverse spin Hall effect.[16] For the magnetoelectric module, three mechanisms have been proposed to accomplish the required function: strain, exchange-coupling, or charge-induced effects.[17–24] Each of these presents advantages and drawbacks; for example, exchange-bias coupling of the magnetoelectric to a ferromagnet implicitly breaks time-reversal symmetry but is an interface mediated coupling mechanism which means that the strength of the coupling is delicate. In contrast, strain-mediated approaches are longer range, but have the disadvantage of not breaking time symmetry and hence are useful in manipulating the magnetic anisotropy. Compared with the two other approaches, strain in composite heterostructures provides the potential for robust coupling in large area and thickness devices,[17,21,25] and has made this approach one of the more attractive options. Numerous studies have explored the potential for magnetoelectric coupling in ferromagnetic/piezoelectric heterostructures including Co/$0.7PbMg_{1/3}Nb_{2/3}O_3$-$0.3PbTiO_3$,[26,27] $Co_{0.4}Fe_{0.4}B_{0.2}$/ $0.7PbMg_{1/3}Nb_{2/3}O_3$-$0.3PbTiO_3$,[18,28] $Fe_{0.5}Rh_{0.5}$/$0.72PbMg_{1/3}Nb_{2/3}O_3$-$0.28PbTiO_3$,[21] etc. These works, however, made use of bulk or thick-film piezoelectrics which require relatively high voltages (typically >250 V, corresponding to 5 kV/cm for 0.5-mm-thick piezoelectrics) and, thus large energies, to actuate and thus do not meet the growing call for low-power, energy-efficient devices.[29]

Here, magnetoelectric coupling is explored in epitaxial multiferroic heterostructures of 30 nm $Fe_{0.5}Rh_{0.5}$ / 100 nm $0.68PbMg_{1/3}Nb_{2/3}O_3$-$0.32PbTiO_3$ (PMN-PT) and 30 nm $Fe_{0.5}Rh_{0.5}$ / 10 nm MgO / 100 nm PMN-PT / 25 nm $Ba_{0.5}Sr_{0.5}RuO_3$ (BSRO) / $NdScO_3$ (NSO) (110) heterostructures.

The thin MgO-buffer layer was employed to protect the PMN-PT thin films during high-temperature $Fe_{0.5}Rh_{0.5}$ deposition in reducing conditions. It is found that in both cases, high-quality, epitaxial, (001)-oriented films of $Fe_{0.5}Rh_{0.5}$ can be grown on the PMN-PT thin films. Subsequent temperature-dependent magnetization and resistivity studies reveal the ability to produce near-room-temperature phase transitions in the $Fe_{0.5}Rh_{0.5}$. A methodology to probe and quantify the magnetoelectric coupling in small thin-film devices via anomalous Hall effect studies is presented wherein one can compare the spin-flop field change induced by temperature and external voltage to extract a measure of the magnetoelectric coupling coefficient. Values approaching ~7.08×10^{-8} s/m at 325 K while applying just -0.75 V bias are achieved. The results demonstrate the potential for near room temperature low-voltage control of magnetism in $Fe_{0.5}Rh_{0.5}$ via piezoelectric strain in PMN-PT thin films. Future directions and possible improvements to these devices are also discussed.

RESULTS AND DISCUSSION

Here, we focus on using $Fe_{0.5}Rh_{0.5}$ to demonstrate the potential for strain-mediated magnetoelectric coupling. This material has received considerable attention as a potential candidate for electrical-field control of magnetization due to its metamagnetic transition from an antiferromagnetic (AFM) phase to a ferromagnetic (FM) phase around $T^* \approx 350$ K.[30–32] Previous studies demonstrated that epitaxial $Fe_{0.5}Rh_{0.5}$ thin films can be grown on single-crystal substates of piezoelectrics such as $BaTiO_3$ and PMN-PT and that field-induced strains from the substrates were able to shift the AFM-to-FM phase transition and induce large electroresistance effects.[17,21] We explored the optimization

1 of $Fe_{0.5}Rh_{0.5}$ growth in three heterostructure variants: 2 nm Pt / 30 nm $Fe_{0.5}Rh_{0.5}$ / MgO (001)
2 (henceforth, $Fe_{0.5}Rh_{0.5}$/MgO; Fig. 1a), 2 nm Pt / 30 nm $Fe_{0.5}Rh_{0.5}$ / 100 nm PMN-PT / 25 nm
3 $Ba_{0.5}Sr_{0.5}RuO_3$ / $NdScO_3$ (110) (henceforth, $Fe_{0.5}Rh_{0.5}$/PMN-PT; Fig. 1b), 2 nm Pt / 30 nm
4 $Fe_{0.5}Rh_{0.5}$ / 10 nm MgO / 100 nm PMN-PT / 25 nm $Ba_{0.5}Sr_{0.5}RuO_3$ / $NdScO_3$ (110) (henceforth,
5 $Fe_{0.5}Rh_{0.5}$/MgO/PMN-PT; Fig. 1c). Growth on MgO (001) substrates was used for internal
6 reference due to the excellent lattice matching between $Fe_{0.5}Rh_{0.5}$ (body-centered cubic, a = 0.423
7 nm) and MgO (rock-salt structure, a = 0.421 nm) and prior works showing that high-quality films
8 can be produced therein.[17,21] Details of the growth optimization are provided (Experimental
9 Section and Suppl. Fig. S1). The PMN-PT films were produced following conditions established
10 in previous studies using pulsed-laser deposition.[33,34] The insertion of the MgO-buffer layer was
11 explored in case the growth of the $Fe_{0.5}Rh_{0.5}$ adversely effected the properties of the PMN-PT.
12 Multiple thicknesses of MgO-buffer layer were explored (3-10 nm; data for growths with 3 nm
13 MgO are also provided, Suppl. Fig. S2), and it was found that the slightly thicker MgO layers
14 provided for a better template layer upon which to produce high-quality $Fe_{0.5}Rh_{0.5}$. Following
15 growth, the films were transferred to a UHV sputter deposition system for the platinum and
16 $Fe_{0.5}Rh_{0.5}$ deposition at high temperatures. In all cases, it was found that high-quality, epitaxial
17 (00l)-oriented $Fe_{0.5}Rh_{0.5}$ films could be produced with the best results corresponding to growth at
18 600°C (Experimental Section, Fig. 1d). Estimates of the $Fe_{0.5}Rh_{0.5}$ quality and ordering can be
19 obtained by comparing the diffraction intensity for the 001- and 002- diffraction conditions,[35] and
20 via this analysis the $Fe_{0.5}Rh_{0.5}$/PMN-PT heterostructures were found to be as good or better than
21 the $Fe_{0.5}Rh_{0.5}$/MgO heterostructures (Suppl. Fig. S3). Subsequent studies of film stoichiometry via

1 Rutherford backscattering spectrometry (Experimental Section) indicate that the films grown at
2 the optimized conditions have chemistry $Fe_{0.49}Rh_{0.51}$ (Fig. 1e), within error, the same as the source
3 target and provided an expected AFM-to-FM phase transition at ~350K.[30,31]

4 Having established the ability to create high-quality, epitaxial $Fe_{0.5}Rh_{0.5}$/PMN-PT
5 heterostructures, we proceeded to explore the magnetic and transport properties as a function of
6 temperature to further gauge the quality of the magnetic layer. Magnetization and resistivity (ρ)
7 studies as a function of temperature show the expected first-order phase transition behavior for all
8 heterostructures (Fig. 2), consistent with previous reports.[17,21] For the $Fe_{0.5}Rh_{0.5}$/MgO
9 heterostructures, the AFM-to-FM phase transition occurs from 280-380 K (mid-point ~330 K) with
10 a hysteresis that is ~40 K wide at the mid-point (Fig. 2a,b). At temperatures below ~250 K, the
11 magnetization is essentially zero, indicating that the $Fe_{0.5}Rh_{0.5}$ has been fully transformed to the
12 AFM phase. This is accompanied by a change in the resistivity (Fig. 2b). These $Fe_{0.5}Rh_{0.5}$/MgO
13 heterostructures compare favorably to similar structures reported in the literature and suggest we
14 have high quality $Fe_{0.5}Rh_{0.5}$ under the optimized growth conditions (Suppl. Fig. S4). For the
15 $Fe_{0.5}Rh_{0.5}$/PMN-PT heterostructures, the larger lattice mismatch between the $Fe_{0.5}Rh_{0.5}$ and
16 potential instability of the PMN-PT to high-temperature growth in reducing environments is found
17 to be detrimental for the manifestation of idealized magnetic and transport properties (Fig. 2c,d).
18 Although no impurity phases were detected from X-ray diffraction, the magnetization studies
19 reveal an additional ferromagnetic phase contribution, as indicated by the non-zero magnetization
20 value observed at low temperatures (< 250 K), the wide temperature range of phase transition, and
21 an enhanced mid-point temperature for the transition (Fig. 2c). This further suppresses the

1 difference between the resistivity of the two states (Fig. 2d). Finally, for the $Fe_{0.5}Rh_{0.5}$/MgO/PMN-
2 PT heterostructures, there is a (partial) improvement of the properties compared to the $Fe_{0.5}Rh_{0.5}$-
3 /PMN-PT heterostructures (Fig. 2e,f). While the width of the phase transition (hysteresis) is still
4 quite diffuse and the mid-point temperature for the transition is enhanced, the magnetization does
5 reach zero at low temperatures; suggesting an improved crystalline quality for the $Fe_{0.5}Rh_{0.5}$ upon
6 inclusion of the MgO-buffer layer. Nonetheless, the resistivity behavior is less clean than for films
7 grown directly on MgO substrates.

8 The magnetic quality of the $Fe_{0.5}Rh_{0.5}$ is only one part of the challenge. For the
9 magnetoelectric function to be produced we must be able to apply electric fields to the piezoelectric
10 PMN-PT and produce strains that drive changes in the magnetization. To gauge how the $Fe_{0.5}Rh_{0.5}$
11 deposition process (high temperature, low oxygen pressure) impacts the PMN-PT we probed the
12 room-temperature leakage behavior of several heterostructure types (Experimental Section and
13 Suppl. Fig. S5). For the $Fe_{0.5}Rh_{0.5}$/PMN-PT heterostructures, large and (fairly) symmetric leakage
14 current-voltage behavior is observed. This is consistent with the diminished magnetization data for
15 these same heterostructures and points to the fact that the high-temperature and reducing growth
16 environment for the $Fe_{0.5}Rh_{0.5}$ likely results in the oxidation of the $Fe_{0.5}Rh_{0.5}$ and deterioration of
17 the PMN-PT that ultimately limits the utility of these heterostructures. This is made more obvious
18 by comparing a test structure of room-temperature deposited platinum as the top contacts to the
19 PMN-PT which show considerably lower leakage current densities, especially under negative bias
20 (applying voltage from the top metal layer to the bottom $Ba_{0.5}Sr_{0.5}RuO_3$). Such structures also
21 show highly asymmetric leakage profiles which is due to the asymmetry of the top metal (platinum)

and bottom $Ba_{0.5}Sr_{0.5}RuO_3$ electrodes. To address this challenge, the MgO-buffer layer was explored and leakage studies of the $Fe_{0.5}Rh_{0.5}$/MgO/PMN-PT heterostructures reveal responses more akin to those of the Pt/PMN-Pt structures; in other words, the thin insulating MgO likely suppresses the oxidation of the $Fe_{0.5}Rh_{0.5}$ and the deterioration of the PMN-PT during the subsequent high-temperature $Fe_{0.5}Rh_{0.5}$ growth. In all, these studies of crystal structure and structural quality, magnetic properties of the $Fe_{0.5}Rh_{0.5}$, and leakage behavior of the devices suggest that it is possible to produce high-quality, epitaxial $Fe_{0.5}Rh_{0.5}$ thin films on PMN-PT thin films and that the inclusion of a thin MgO layer both improves the $Fe_{0.5}Rh_{0.5}$ quality and suppresses deterioration of the PMN-PT films during high-temperature, low-pressure $Fe_{0.5}Rh_{0.5}$ growth.

Having established the quality of the $Fe_{0.5}Rh_{0.5}$/MgO and $Fe_{0.5}Rh_{0.5}$/MgO/PMN-PT heterostructures, we focus on these two heterostructures types as we explore methodologies to probe magnetoelectric coupling in micron-scale devices. Since the $Fe_{0.5}Rh_{0.5}$ simultaneously serves as the active magnetic layer and the top electrode it must be defined into small devices sizes, thus making use of traditional magnetic probes (such as magnetometry) challenging. Alternatively, we can leverage magnetotransport approaches and especially the anomalous Hall effect (AHE) to probe the magnetoelectric coupling instead of relying on direct measurements of magnetization under applied electric fields. To probe the AHE, the $Fe_{0.5}Rh_{0.5}$/MgO and $Fe_{0.5}Rh_{0.5}$/MgO/PMN-PT heterostructures were fabricated into Hall bars (~5 μm x 15 μm in size; Experimental Section and Fig. 3a). Before quantifying the magnetoelectric coupling, we first measured temperature-dependent AHE curves for the $Fe_{0.5}Rh_{0.5}$/MgO (Fig. 3b) and $Fe_{0.5}Rh_{0.5}$/MgO/PMN-PT (Fig. 3c) heterostructures. The $Fe_{0.5}Rh_{0.5}$/MgO heterostructures serve as a reference for the AHE changes

during the AFM-to-FM phase transition in $Fe_{0.5}Rh_{0.5}$. At 250 K, the $Fe_{0.5}Rh_{0.5}$ in both heterostructures is in the pure AFM phase with negligible magnetization and, hence, the ordinary Hall effect dominates the transport. As the temperature increases, the Hall resistivity (ρ_{xy}) of the $Fe_{0.5}Rh_{0.5}$ becomes dominated by contributions from the AHE, which indicates that the AFM-to-FM phase transition has been initiated upon increasing temperature. As a result, ρ_{xy} increases with magnetic field and falls back with decreasing magnetic field. Both the $Fe_{0.5}Rh_{0.5}$/MgO and $Fe_{0.5}Rh_{0.5}$/MgO/PMN-PT heterostructures behave similarly in nature, but with the temperature for the onset of and completion of the AFM-to-FM transition being higher in the $Fe_{0.5}Rh_{0.5}$/MgO/PMN-PT heterostructure.

As it pertains to the magnetoelectric coupling, the ultimate goal is to produce a quantitative estimate of the magnetoelectric coupling coefficient $\alpha_{ME} = \mu_0 \frac{\Delta M}{E}$ where M is the magnetization and E is the applied electric field. While E can be readily understood from the applied voltage and device geometry, the estimation of ΔM poses a challenge due to the lack of direct measurements of magnetization in the small volume/area devices. To overcome this challenge, we leveraged the linear temperature-dependence of the spin-flop field (SFF, the magnetic field at which a spin-flop transition occurs) extracted from the temperature-dependent Hall-resistivity studies (Fig. 3d). Again, the nature of the two heterostructures is the same with nearly identical slopes for the response with varying temperature. Therefore, we can use this information to estimate the ΔM value under a given E by first finding the temperature which is expected to have the same SFF as the SFF under the applied E. In turn, the difference in temperature is then converted to an estimated ΔM using the magnetization-temperature curves from the same heterostructures (Fig. 2).

1 To quantify α_{ME}, negative voltages were applied to the $Fe_{0.5}Rh_{0.5}$/MgO/PMN-PT
2 heterostructures and the resulting magnetotransport was measured at 325 K (Experimental Section,
3 Fig. 4a). Of course, there is no effect in the $Fe_{0.5}Rh_{0.5}$/MgO heterostructures and similar
4 experiments were tried for the $Fe_{0.5}Rh_{0.5}$/PMN-PT, but the large leakage effects limited their utility
5 (Suppl. Fig. S6). The ρ_{xy} curves reveal signs of voltage dependence in that the SFF increases with
6 increasing magnitude of applied voltage (Fig. 4a), which indicates that the AFM-to-FM phase
7 transition occurs at different fields under applied voltage. Observable changes in AHE can even
8 be seen at -0.5 V (-50 kV/cm), which saturate at -0.75 V (-75 kV/cm). Using the aforementioned
9 linear relationship between SFF and temperature (Fig. 3d), the SFF changes at 325 K for the
10 $Fe_{0.5}Rh_{0.5}$/MgO/PMN-PT heterostructures under different voltages are used to estimate the
11 temperature at which the $Fe_{0.5}Rh_{0.5}$ has the same SFF. The difference between the magnetization
12 at this temperature and the magnetization at 325 K (δM) is then extracted from the magnetization-
13 temperature curves (Fig. 2e); a summary of the pertinent values of important terms (*i.e.*, applied
14 voltage, SFF at 325 K, the equivalent temperature for the same SFF at 0 V, the estimated δM, and
15 the extracted α_{ME}) are provided (Fig. 4b). The extracted α_{ME} as a function of negative voltage
16 shows a sharp increase between -0.5 and -0.75 V and reaches a value of 5.29 x 10^{-9} s/m at 325 K
17 at the maximum (Fig. 4c). At higher voltages, further changes in the AHE are not observed, likely
18 due to the potential leakage at high electric fields and/or saturation of the piezoelectric strain of
19 the films.

20 The observed values of α_{ME} can be compared to prior works on bulk crystals and thin films
21 (Fig. 5). Ideally, the combination of low voltage (< 100 mV) actuation, room-temperature (300 K)

functionality, and resulting large α_{ME} characteristics are desired. As the large scatter in the data suggests, however, this is a challenging task. Although $Fe_{0.5}Rh_{0.5}$/MgO/PMN-PT heterostructures satisfy the low voltage (-0.75 V) and near room-temperature (325 K) characteristics, they suffer from relatively small α_{ME}, which are likely ultimately due to the reduced piezoelectric strains that are possible in clamped films[36] and due to the thin (relatively lower dielectric constant) MgO-buffer layer which is required to address issues in integrating the metal ferromagnetic layer with PMN-PT across which some of the voltage is dropping. To demonstrate the potential of further improvements in thin films, we estimate the effective α_{ME} based on the actual voltage drop across PMN-PT layer. Here, the actual voltage drops in MgO (dielectric permittivity of 8) and PMN-PT (dielectric permittivity of 1000) layer can be estimated from charge continuity conditions at the interface.[34] Using these values, when -0.75 V is applied to the device, the voltage drops across the MgO and PMN-PT layers are estimated to be -0.694 V and -0.056 V, respectively. Using this rather simple estimation, one obtains an effective α_{ME} of 7.08×10^{-8} s/m at 325 K, which are comparable to α_{ME} obtained from using single-crystal $BaTiO_3$ and 0.72PMN-0.28PT substrates.[37,38] We expect that progress in the fabrication of laterally defined structures (thereby removing some of the in-plane clamping of the films) and the integration of piezoelectric membranes released from the substrate[39,40] and improvements in the growth process[41] can lead to further refinements of the magnetoelectric response.

CONCLUSIONS

In summary, it has been shown that it is possible to translate similar magnetoelectric

1 heterostructures studied in the bulk to the thin film regime. It is possible to produce high-quality,
2 epitaxial, (001)-oriented films of $Fe_{0.5}Rh_{0.5}$ on PMN-PT and MgO/PMN-PT thin films. Subsequent
3 temperature-dependent magnetization and resistivity studies reveal the ability to produce near-
4 room-temperature phase transitions in the $Fe_{0.5}Rh_{0.5}$. A methodology to probe and quantify the
5 magnetoelectric coupling in small thin-film devices via anomalous Hall effect studies was also
6 developed wherein one can compare the spin-flop field change induced by temperature and
7 external voltage to extract a measure of the magnetoelectric coupling coefficient. Using this
8 approach, α_{ME} was estimated to be 5.29 x 10^{-9} s/m at 325 K under -0.75 V and as large as 7.08 x
9 10^{-8} s/m if one accounts for the voltage drop only across the PMN-PT. While this is promising for
10 next-generation electric-field control of magnetization, improvements in how we integrate the
11 dissimilar materials are needed and nanofabrication approaches to enable large piezoelectric
12 responses in thin films are needed.

1 **EXPERIMENTAL SECTION**

2 **Epitaxial thin-film synthesis.** Pulsed-laser deposition (PLD) using a KrF excimer laser
3 (248 nm, LPX 300, Coherent) was used to grow 100 nm $0.68Pb(Mg_{1/3}Nb_{2/3})O_3$-$0.32PbTiO_3$ (PMN-
4 PT) / 25 nm $Ba_{0.5}Sr_{0.5}RuO_3$ (BSRO) heterostructures on $NdScO_3$ (NSO) (110) substrates (CrysTec
5 GmbH). The PMN-PT growth was carried out at a heater temperature of 600 °C in a dynamic
6 oxygen pressure of 200 mTorr with a laser fluence of 1.8 J/cm^2 and a laser repetition rate of 2 Hz
7 from a ceramic target (Praxair) of the same composition with 10% lead excess to compensate for
8 lead loss during growth. The BSRO growth was carried out at temperature of 750 °C in a dynamic
9 oxygen pressure of 20 mTorr with a laser fluence of 1.85 J/cm^2 and a laser repetition rate of 3 Hz
10 from a ceramic target (Praxair) of the same composition. Following the growth, the samples were
11 cooled to room temperature at 5°C/min. in a static oxygen pressure of 700 Torr. In the case of
12 MgO-buffered heterostructures, 3-10 nm MgO buffer layer was grown by PLD immediately after
13 PMN-PT at the PMN-PT growth temperature of 600 °C in a dynamic oxygen pressure of 20 mTorr
14 with a laser fluence of 2.5 J/cm^2 and a laser repetition rate of 15 Hz from a ceramic target (Praxair)
15 of the same composition. $Fe_{0.5}Rh_{0.5}$ films were grown using DC sputtering techniques. For the
16 sputtering deposition of $Fe_{0.5}Rh_{0.5}$, the PMN-PT / BSRO / NSO heterostructures were heated to
17 500-700 °C in a base pressure of at least 10^{-8} Torr. Subsequently, a small amount of argon gas was
18 introduced into the chamber, maintaining the total pressure at 3.0 mTorr. The $Fe_{0.5}Rh_{0.5}$ films were
19 then grown from a stoichiometric $Fe_{0.5}Rh_{0.5}$ target. After the deposition, films were annealed at
20 various temperatures between 600 and 800 °C in vacuum for 40 min. and subsequently cooled to
21 room temperature at 10 °C/min. 3 nm thick capping platinum layers were also grown by DC

sputtering at room-temperature and a target power of 100 W in a dynamic argone pressure of 2 mTorr to prevent the oxidation of FeRh.

Structural characterization. X-ray θ-2θ line scans about symmetrical reflections of the films and substrates were conducted with a high-resolution X-ray diffractometer (X'pert Pro2, PANalytical).

Magnetometry. Magnetic characterizations were carried out with a superconducting quantum interference device magnetometer (Quantum Design, 2 K, 7 T), with the magnetic field applied along the out-of-plane direction of the film.

Transport measurements. The temperature-dependent resistance and Hall effect measurement were carried out in a CRYOGENIC measurement system (2 K, 14 T) with the magnetic field applied perpendicular to the device plane. A constant 10 μA dc current was applied for all temperature-dependent resistivity measurements. A constant 100 μA dc current was applied for all Hall measurements with a series of back gating voltages.

Device fabrication for AHE studies. To measure the physical properties of the $Fe_{0.5}Rh_{0.5}$ / (MgO) / PMN-PT heterostructures, the active region was patterned into a 6-point contact Hall bar geometry (20 μm × 400 μm) by the following fabrication process. First, photoresist was patterned by spin-coating on the blanket Pt/ $Fe_{0.5}Rh_{0.5}$ / (MgO) / PMN-PT heterostructures. Second, the photoresist was patterned into Hall-bar geometries via standard optical photolithography. Third, the heterostructures were ion-milled to define the active region. Fourth, a 300-nm-thick insulating layer of MgO was deposited at room-temperature by PLD to separate the bottom contacts from the top contacts. Fifth, the photoresist was removed in acetone and a second photoresist layer was spin-coated for the second photolithography step. Sixth, inverse patterns of platinum contact pads were formed by photolithography. Seventh, a 100-nm-thick layer of platinum was deposited to

form contact pads. Eighth, the photoresist was removed in acetone. Ninth, the heterostructures were mounted on a chip carrier and wire-bonded for insertion in the measurement system.

ACKNOWLEDGEMENTS:

W.Z. and J.K. contributed equally to the work. W.Z., J.K., and L.W.M. acknowledge the Intel Corp. via the FEINMAN program. X.H and R.R. acknowledge the support of ASCENT, one of the SRC-JUMP Centers. D.P. acknowledges funding from the European Union's Horizon 2020 research and innovation program under the Marie Skłodowska-Curie grant agreement No. 79712. G.A.P.V. acknowledges support from the National Science Foundation under grant DMR-1708615 and from the NSF GRFP

1 **Figures/Captions**

2

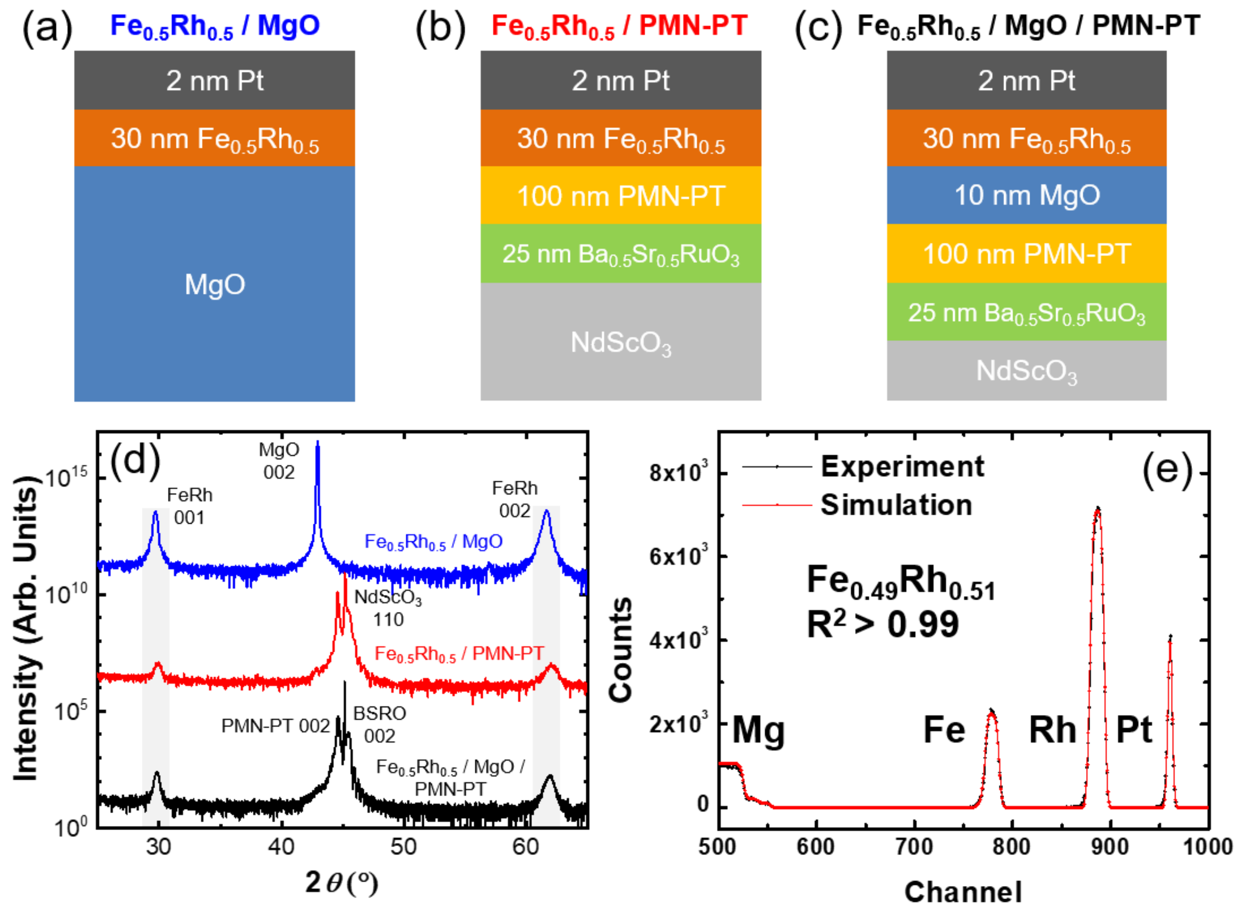

3 **Figure 1.** Schematic illustrations of the three heterostructure variants used and described in this
4 work including the (a) $Fe_{0.5}Rh_{0.5}$/MgO, (b) $Fe_{0.5}Rh_{0.5}$/PMN-PT, and (c) $Fe_{0.5}Rh_{0.5}$/MgO/PMN-PT
5 structures. (d) θ-2θ X-ray diffraction scans for the same three heterostructure variants revealing
6 the ability to produce fully epitaxial, 00*l*-oriented films of $Fe_{0.5}Rh_{0.5}$ in all cases. (e) Rutherford
7 backscattering spectrometry spectra for an as-grown $Fe_{0.5}Rh_{0.5}$/MgO heterostructure at the
8 optimized growth condition.

9

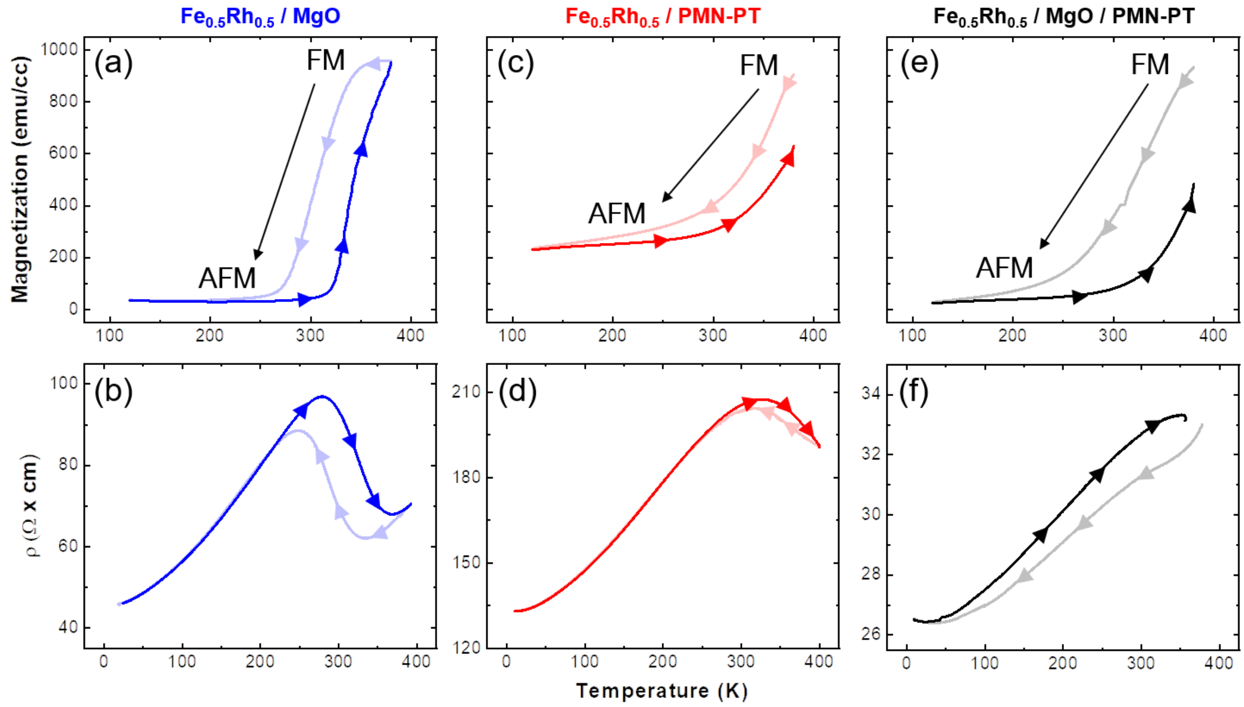

1 **Figure 2.** Magnetization and resistivity data as a function of temperature for the as-grown
2 heterostructures, including (a) magnetization and (b) transport data for the $Fe_{0.5}Rh_{0.5}$/MgO
3 heterostructures, (c) magnetization and (d) transport data for the $Fe_{0.5}Rh_{0.5}$/PMN-PT
4 heterostructures, and (e) magnetization and (f) transport data for the $Fe_{0.5}Rh_{0.5}$/MgO/PMN-PT
5 heterostructures.

6

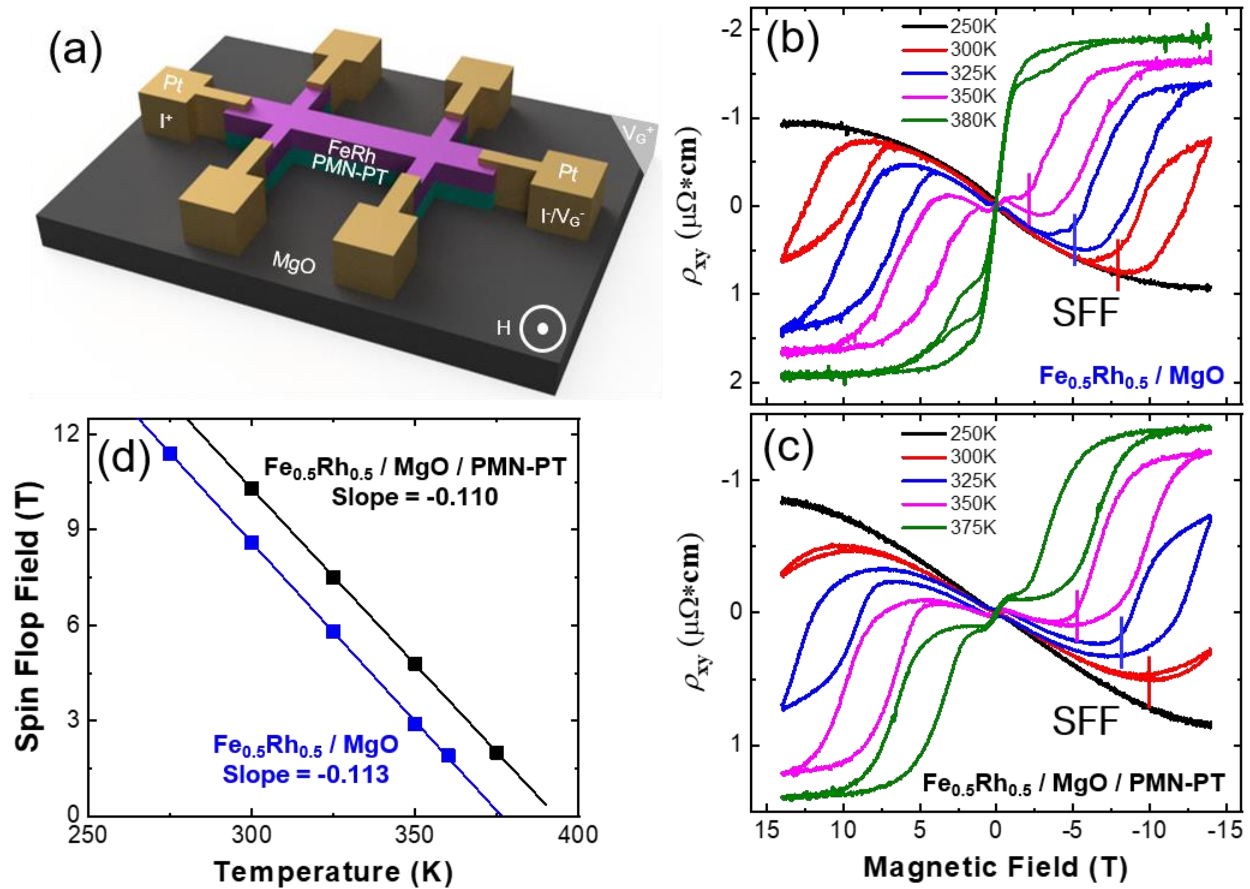

Figure 3. (a) Schematic illustration of the Hall-bar devices fabricated into the various heterostructures. Anomalous Hall resistivity as a function of applied magnetic field at various temperatures for the (b) $Fe_{0.5}Rh_{0.5}$/MgO and (c) $Fe_{0.5}Rh_{0.5}$/MgO/PMN-PT heterostructures. (d) Summary of the spin-flop field (SFF) as a function of temperature for the different heterostructure variants revealing similar temperature-dependence for both heterostructures.

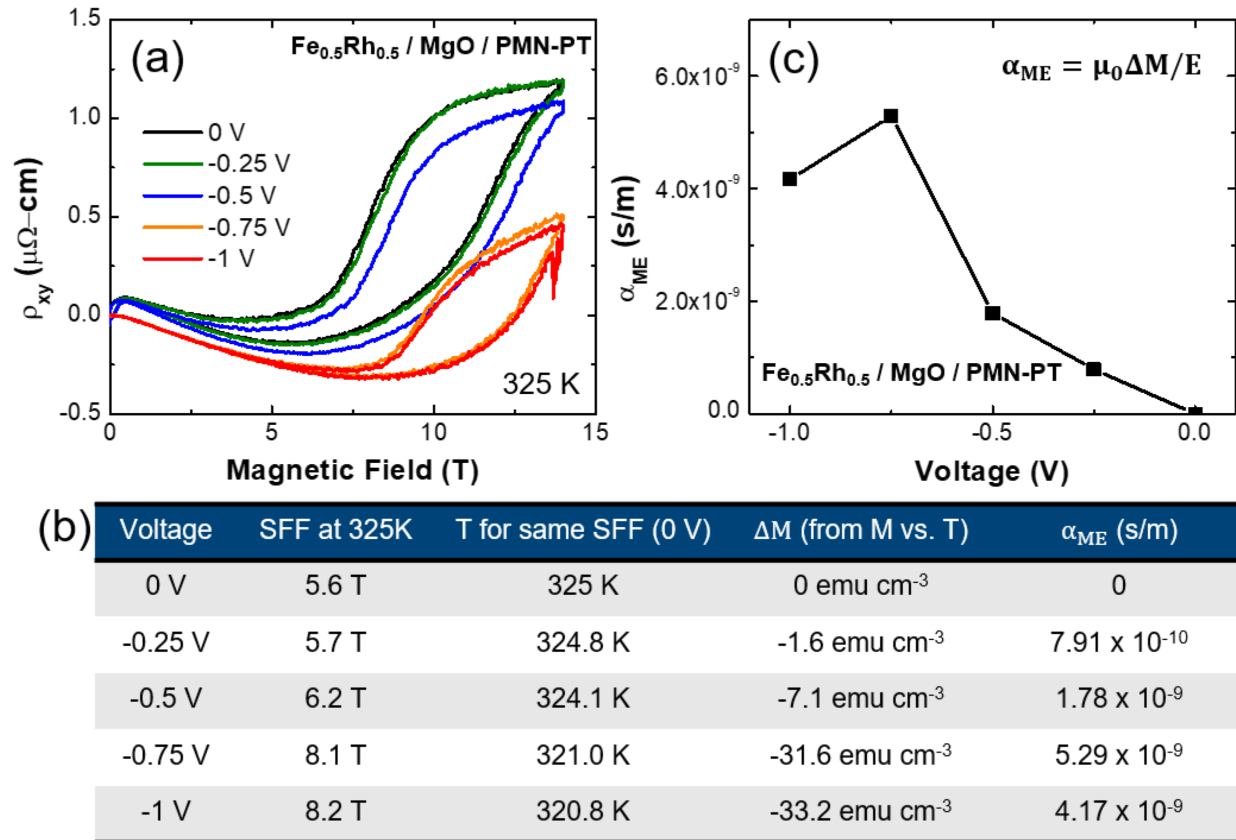

Voltage	SFF at 325K	T for same SFF (0 V)	ΔM (from M vs. T)	α_{ME} (s/m)
0 V	5.6 T	325 K	0 emu cm^{-3}	0
-0.25 V	5.7 T	324.8 K	-1.6 emu cm^{-3}	7.91 x 10^{-10}
-0.5 V	6.2 T	324.1 K	-7.1 emu cm^{-3}	1.78 x 10^{-9}
-0.75 V	8.1 T	321.0 K	-31.6 emu cm^{-3}	5.29 x 10^{-9}
-1 V	8.2 T	320.8 K	-33.2 emu cm^{-3}	4.17 x 10^{-9}

Figure 4. (a) Anomalous Hall resistivity as a function of magnetic field measured at different applied dc voltages for the $Fe_{0.5}Rh_{0.5}$/MgO/PMN-PT heterostructures reveals a strong magnetoelectric effect with a sharp raise in magnitude between -0.5 and -0.75 V. (b) Summary of important values from both the magnetization and transport studies to estimate the magnetoelectric coupling. (c) Evolution of the magnetoelectric coupling coefficient α_{ME} as a function of applied voltage in this system.

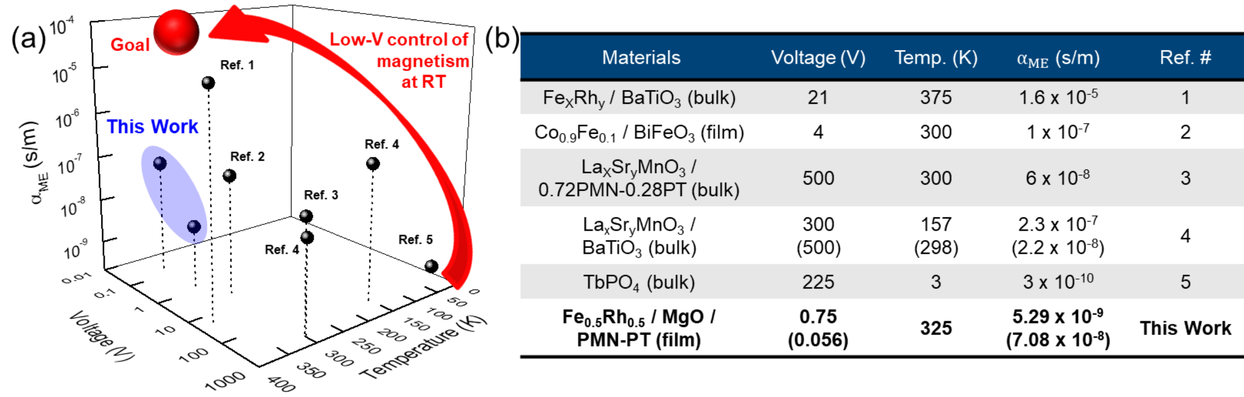

Materials	Voltage (V)	Temp. (K)	α_{ME} (s/m)	Ref. #
Fe_XRh_y / $BaTiO_3$ (bulk)	21	375	1.6×10^{-5}	1
$Co_{0.9}Fe_{0.1}$ / $BiFeO_3$ (film)	4	300	1×10^{-7}	2
$La_XSr_yMnO_3$ / 0.72PMN-0.28PT (bulk)	500	300	6×10^{-8}	3
$La_xSr_yMnO_3$ / $BaTiO_3$ (bulk)	300 (500)	157 (298)	2.3×10^{-7} (2.2×10^{-8})	4
$TbPO_4$ (bulk)	225	3	3×10^{-10}	5
$Fe_{0.5}Rh_{0.5}$ / MgO / PMN-PT (film)	**0.75 (0.056)**	**325**	**5.29×10^{-9} (7.08×10^{-8})**	**This Work**

Figure 5. (a) Graphical and (b) table summary of studies of magnetoelectric coupling coefficient α_{ME} in ferromagnetic/piezoelectric-ferroelectric heterostructures (including both bulk and thin-film forms). The ultimate goal is a combination of low-voltage, room-temperature, and high α_{ME} which remains challenging to obtain. Pertinent references include: 1) R. Cherifi, *et al. Nature Mater*. **13**, 345–351 (2014); 2) J. Heron, *et al. Nature* **516**, 370–373 (2014).; 3) C. Thiele, *et al. Phys. Rev. B* **75**, 054408 (2007); 4) W. Eerenstein, *et al. Nature Mater*. **6**, 348–351 (2007); and 5) G. T. Rado, *et al. Phys. Rev. B* 29, 4041 (1984).

REFERENCES

(1) Moore, G. E. Cramming More Components Onto Integrated Circuits. *P IEEE* **1998**, *86* (1), 82–85. https://doi.org/10.1109/jproc.1998.658762.

(2) Dennard, R. H.; Gaensslen, F. H.; Yu, H.-N.; Rideout, V. L.; Bassous, E.; Leblanc, A. R. Design Of Ion-Implanted MOSFET's with Very Small Physical Dimensions. *P IEEE* **1999**, *87* (4), 668–678. https://doi.org/10.1109/jproc.1999.752522.

(3) Khan, H. N.; Hounshell, D. A.; Fuchs, E. R. H. Science and Research Policy at the End of Moore's Law. *Nat. Electron.* **2018**, *1* (1), 14–21. https://doi.org/10.1038/s41928-017-0005-9.

(4) Nikonov, D. E.; Young, I. A. Benchmarking of Beyond-CMOS Exploratory Devices for Logic Integrated Circuits. *Ieee J Explor Solid-state Comput. Devices Circuits* **2015**, *1*, 3–11. https://doi.org/10.1109/jxcdc.2015.2418033.

(5) Manipatruni, S.; Nikonov, D. E.; Young, I. A. Beyond CMOS Computing with Spin and Polarization. *Nat. Phy.s* **2018**, *14* (4), 338–343. https://doi.org/10.1038/s41567-018-0101-4.

(6) Nikonov, D. E.; Young, I. A. Overview of Beyond-CMOS Devices and a Uniform Methodology for Their Benchmarking. *P IEEE* **2013**, *101* (12), 2498–2533. https://doi.org/10.1109/jproc.2013.2252317.

(7) Nikonov, D. E.; Bourianoff, G. I.; Ghani, T. Proposal of a Spin Torque Majority Gate Logic. *IEEE Electr. Device Lett.* **2011**, *32* (8), 1128–1130. https://doi.org/10.1109/led.2011.2156379.

(8) Behin-Aein, B.; Datta, D.; Salahuddin, S.; Datta, S. Proposal for an All-Spin Logic Device with Built-in Memory. *Nat. Nanotechnol.* **2010**, *5* (4), 266–270. https://doi.org/10.1038/nnano.2010.31.

(9) Imre, A.; Csaba, G.; Ji, L.; Orlov, A.; Bernstein, G. H.; Porod, W. Majority Logic Gate for Magnetic Quantum-Dot Cellular Automata. *Science* **2006**, *311* (5758), 205–208. https://doi.org/10.1126/science.1120506.

(10) Avci, U. E.; Rios, R.; Kuhn, K.; Young, I. A. Comparison of Performance, Switching Energy and Process Variations for the TFET and MOSFET in Logic. *2011 Symposium on VLSI Technology Digest of Tech. Pap.* **2011**.

(11) Ionescu, A. M.; Riel, H. Tunnel Field-Effect Transistors as Energy-Efficient Electronic Switches. *Nature* **2011**, *479* (7373), 329–337. https://doi.org/10.1038/nature10679.

(12) Salahuddin, S.; Datta, S. Use of Negative Capacitance to Provide Voltage Amplification for Low Power Nanoscale Devices. *Nano Lett.* **2008**, *8* (2), 405–410. https://doi.org/10.1021/nl071804g.

(13) Newns, D.; Elmegreen, B.; Liu, X. H.; Martyna, G. A Low-Voltage High-Speed Electronic Switch Based on Piezoelectric Transduction. *J. Appl. Phys.* **2012**, *111* (8), 084509. https://doi.org/10.1063/1.4704391.

(14) Calayir, V.; Nikonov, D. E.; Manipatruni, S.; Young, I. A. Static and Clocked Spintronic Circuit Design and Simulation with Performance Analysis Relative to CMOS. *IEEE Trans. Circuits Syst. Regul. Pap.* **2014**, *61* (2), 393–406. https://doi.org/10.1109/tcsi.2013.2268375.

(15) Hellman, F.; Hoffmann, A.; Tserkovnyak, Y.; Beach, G. S. D.; Fullerton, E. E.; Leighton, C.; MacDonald, A. H.; Ralph, D. C.; Arena, D. A.; Dürr, H. A.; Fischer, P.; Grollier, J.; Heremans, J. P.; Jungwirth, T.; Kimel, A. V.; Koopmans, B.; Krivorotov, I. N.; May, S. J.; Petford-Long, A. K.; Rondinelli, J. M.; Samarth, N.; Schuller, I. K.; Slavin, A. N.; Stiles, M. D.; Tchernyshyov, O.; Thiaville, A.; Zink, B. L. Interface-Induced Phenomena in Magnetism. *Rev. Mod. Phys.* **2017**, *89* (2), 025006. https://doi.org/10.1103/revmodphys.89.025006.

(16) Manipatruni, S.; Nikonov, D. E.; Lin, C.-C.; Gosavi, T. A.; Liu, H.; Prasad, B.; Huang, Y.-L.; Bonturim, E.; Ramesh, R.; Young, I. A. Scalable Energy-Efficient Magnetoelectric Spin–Orbit Logic. *Nature* **2019**, *565* (7737), 35–42. https://doi.org/10.1038/s41586-018-0770-2.

(17) Cherifi, R. O.; Ivanovskaya, V.; Phillips, L. C.; Zobelli, A.; Infante, I. C.; Jacquet, E.; Garcia, V.; Fusil, S.; Briddon, P. R.; Guiblin, N.; Mougin, A.; Ünal, A. A.; Kronast, F.; Valencia, S.; Dkhil, B.; Barthélémy, A.; Bibes, M. Electric-Field Control of Magnetic Order above Room Temperature. *Nat. Mater.* **2014**, *13* (4), 345–351. https://doi.org/10.1038/nmat3870.

(18) Zhang, S.; Zhao, Y. G.; Li, P. S.; Yang, J. J.; Rizwan, S.; Zhang, J. X.; Seidel, J.; Qu, T. L.; Yang, Y. J.; Luo, Z. L.; He, Q.; Zou, T.; Chen, Q. P.; Wang, J. W.; Yang, L. F.; Sun, Y.; Wu, Y. Z.; Xiao, X.; Jin, X. F.; Huang, J.; Gao, C.; Han, X. F.; Ramesh, R. Electric-Field Control of Nonvolatile Magnetization in $Co_{40}Fe_{40}B_{20}/Pb(Mg_{1/3}Nb_{2/3})_{0.7}Ti_{0.3}O_3$ Structure at Room Temperature. *Phys. Rev. Lett.* **2011**, *108* (13), 137203. https://doi.org/10.1103/physrevlett.108.137203.

(19) He, X.; Wang, Y.; Wu, N.; Caruso, A. N.; Vescovo, E.; Belashchenko, K. D.; Dowben, P. A.; Binek, C. Robust Isothermal Electric Control of Exchange Bias at Room Temperature. *Nat. Mater.* **2010**, *9* (7), 579–585. https://doi.org/10.1038/nmat2785.

(20) Heron, J. T.; Bosse, J. L.; He, Q.; Gao, Y.; Trassin, M.; Ye, L.; Clarkson, J. D.; Wang, C.; Liu, J.; Salahuddin, S.; Ralph, D. C.; Schlom, D. G.; Íñiguez, J.; Huey, B. D.; Ramesh, R.

Deterministic Switching of Ferromagnetism at Room Temperature Using an Electric Field. *Nature* **2014**, *516* (7531), 370–373. https://doi.org/10.1038/nature14004.

(21) Lee, Y.; Liu, Z. Q.; Heron, J. T.; Clarkson, J. D.; Hong, J.; Ko, C.; Biegalski, M. D.; Aschauer, U.; Hsu, S. L.; Nowakowski, M. E.; Wu, J.; Christen, H. M.; Salahuddin, S.; Bokor, J. B.; Spaldin, N. A.; Schlom, D. G.; Ramesh, R. Large Resistivity Modulation in Mixed-Phase Metallic Systems. *Nat. Commun.* **2015**, *6* (1), 5959. https://doi.org/10.1038/ncomms6959.

(22) Conte, R. L.; Gorchon, J.; Mougin, A.; Lambert, C. H. A.; El-Ghazaly, A.; Scholl, A.; Salahuddin, S.; Bokor, J. Electrically Controlled Switching of the Magnetization State in Multiferroic $BaTiO_3$/CoFe Submicrometer Structures. *Phys. Rev. Mater.* **2018**, *2* (9), 091402. https://doi.org/10.1103/physrevmaterials.2.091402.

(23) Spaldin, N. A.; Fiebig, M. The Renaissance of Magnetoelectric Multiferroics. *Science* **2005**, *309* (5733), 391–392. https://doi.org/10.1126/science.1113357.

(24) Fiebig, M. Revival of the Magnetoelectric Effect. *J. Phys. D Appl. Phys.* **2005**, *38* (8), R123. https://doi.org/10.1088/0022-3727/38/8/r01.

(25) Zhao, W.; Zhang, D.; Meng, D.; Huang, W.; Feng, L.; Hou, C.; Lu, Y.; Yin, Y.; Li, X. Electric-Field-Controlled Nonvolatile Magnetic Switching and Resistive Change in $La_{0.6}Sr_{0.4}MnO_3$/0.7$Pb(Mg_{1/3}Nb_{2/3})O_3$-0.3$PbTiO_3$ (011) Heterostructure at Room Temperature. *Appl. Phys. Lett.* **2016**, *109* (26), 263502. https://doi.org/10.1063/1.4973355.

(26) Yang, S.; Peng, R.; Jiang, T.; Liu, Y.; Feng, L.; Wang, J.; Chen, L.; Li, X.; Nan, C. Non-Volatile 180° Magnetization Reversal by an Electric Field in Multiferroic Heterostructures. *Adv. Mater.* **2014**, *26* (41), 7091–7095. https://doi.org/10.1002/adma.201402774.

(27) Yang, S.; Feng, L.; Zhang, D.; Huang, W.; Dong, S.; Wang, J.; Zou, L.; Li, X.; Nan, C. Magnetically Correlated Anisotropic Resistive Switching Manipulated by Electric Field in Co/PMN-PT Heterostructures. *J. Alloy. Compd.* **2015**, *646*, 472–476. https://doi.org/10.1016/j.jallcom.2015.04.239.

(28) Zhang, S.; Zhao, Y.; Xiao, X.; Wu, Y.; Rizwan, S.; Yang, L.; Li, P.; Wang, J.; Zhu, M.; Zhang, H.; Jin, X.; Han, X. Giant Electrical Modulation of Magnetization in $Co_{40}Fe_{40}B_{20}/Pb(Mg_{1/3}Nb_{2/3})_{0.7}Ti_{0.3}O_3$ (011) Heterostructure. *Sci. Rep.* **2014**, *4* (1), 3727. https://doi.org/10.1038/srep03727.

(29) Cheng, Y.; Peng, B.; Hu, Z.; Zhou, Z.; Liu, M. Recent Development and Status of Magnetoelectric Materials and Devices. *Phys. Lett. A* **2018**, *382* (41), 3018–3025. https://doi.org/10.1016/j.physleta.2018.07.014.

(30) Swartzendruber, L. J. The Fe−Rh (Iron-Rhodium) System. *Bulletin Alloy Phase Diagrams* **1984**, *5* (5), 456–462. https://doi.org/10.1007/bf02872896.

(31) Moruzzi, V. L.; Marcus, P. M. Antiferromagnetic-Ferromagnetic Transition in FeRh. *Phys. Rev. B* **1992**, *46* (5), 2864–2873. https://doi.org/10.1103/physrevb.46.2864.

(32) Suzuki, I.; Naito, T.; Itoh, M.; Sato, T.; Taniyama, T. Clear Correspondence between Magnetoresistance and Magnetization of Epitaxially Grown Ordered FeRh Thin Films. *J. Appl. Phys.* **2011**, *109* (7), 07C717. https://doi.org/10.1063/1.3556754.

(33) Kim, J.; Saremi, S.; Acharya, M.; Velarde, G.; Parsonnet, E.; Donahue, P.; Qualls, A.; Garcia, D.; Martin, L. W. Ultrahigh Capacitive Energy Density in Ion-Bombarded Relaxor Ferroelectric Films. *Science* **2020**, *369* (6499), 81–84. https://doi.org/10.1126/science.abb0631.

(34) Kim, J.; Takenaka, H.; Qi, Y.; Damodaran, A. R.; Fernandez, A.; Gao, R.; McCarter, M. R.; Saremi, S.; Chung, L.; Rappe, A. M.; Martin, L. W. Epitaxial Strain Control of Relaxor Ferroelectric Phase Evolution. *Adv. Mater.* **2019**, *31* (21), 1901060. https://doi.org/10.1002/adma.201901060.

(35) Kande, D.; Pisana, S.; Weller, D.; Laughlin, D. E.; Zhu, J.-G. Enhanced B2 Ordering of FeRh Thin Films Using B2 NiAl Underlayers. *IEEE T. Magn.* **2011**, *47* (10), 3296–3299. https://doi.org/10.1109/tmag.2011.2157963.

(36) Nagarajan, V.; Ganpule, C. S.; Nagaraj, B.; Aggarwal, S.; Alpay, S. P.; Roytburd, A. L.; Williams, E. D.; Ramesh, R. Effect of Mechanical Constraint on the Dielectric and Piezoelectric Behavior of Epitaxial $Pb(Mg_{1/3}Nb_{2/3})O_3$(90%)–$PbTiO_3$(10%) Relaxor Thin Films. *Appl. Phys. Lett.* **1999**, *75* (26), 4183–4185. https://doi.org/10.1063/1.125576.

(37) Eerenstein, W.; Wiora, M.; Prieto, J. L.; Scott, J. F.; Mathur, N. D. Giant Sharp and Persistent Converse Magnetoelectric Effects in Multiferroic Epitaxial Heterostructures. *Nat. Mater.* **2007**, *6* (5), 348–351. https://doi.org/10.1038/nmat1886.

(38) Thiele, C.; Dörr, K.; Bilani, O.; Rödel, J.; Schultz, L. Influence of Strain on the Magnetization and Magnetoelectric Effect in $La_{0.7}A_{0.3}MnO_3$/PMN-PT (001) (A=Sr,Ca). *Phys. Rev. B* **2007**, *75* (5), 054408. https://doi.org/10.1103/physrevb.75.054408.

(39) Kum, H. S.; Lee, H.; Kim, S.; Lindemann, S.; Kong, W.; Qiao, K.; Chen, P.; Irwin, J.; Lee, J. H.; Xie, S.; Subramanian, S.; Shim, J.; Bae, S.-H.; Choi, C.; Ranno, L.; Seo, S.; Lee, S.; Bauer, J.; Li, H.; Lee, K.; Robinson, J. A.; Ross, C. A.; Schlom, D. G.; Rzchowski, M. S.; Eom, C.-B.; Kim, J. Heterogeneous Integration of Single-Crystalline Complex-Oxide Membranes. *Nature* **2020**, *578* (7793), 75–81. https://doi.org/10.1038/s41586-020-1939-z.

1 (40) Pesquera, D.; Parsonnet, E.; Qualls, A.; Xu, R.; Gubser, A. J.; Kim, J.; Jiang, Y.; Velarde,
2 G.; Huang, Y.; Hwang, H. Y.; Ramesh, R.; Martin, L. W. Beyond Substrates: Strain Engineering
3 of Ferroelectric Membranes. *Adv. Mater.* **2020**, *32* (43), 2003780.
4 https://doi.org/10.1002/adma.202003780.

5 (41) Baek, S. H.; Park, J.; Kim, D. M.; Aksyuk, V. A.; Das, R. R.; Bu, S. D.; Felker, D. A.;
6 Lettieri, J.; Vaithyanathan, V.; Bharadwaja, S. S. N.; Bassiri-Gharb, N.; Chen, Y. B.; Sun, H. P.;
7 Folkman, C. M.; Jang, H. W.; Kreft, D. J.; Streiffer, S. K.; Ramesh, R.; Pan, X. Q.; Trolier-
8 McKinstry, S.; Schlom, D. G.; Rzchowski, M. S.; Blick, R. H.; Eom, C. B. Giant Piezoelectricity
9 on Si for Hyperactive MEMS. *Science* **2011**, *334* (6058), 958–961.
10 https://doi.org/10.1126/science.1207186.

11